Quadrupole and octupole collectivity in ^{143}Ba

C. Morse,[1] A. O. Macchiavelli,[1] H. L. Crawford,[1] S. Zhu,[2,3] C. Y. Wu,[4] Y. Y. Wang,[5] J. Meng,[5,6] B. B. Back,[2] B. Bucher,[7] C. M. Campbell,[1] M. P. Carpenter,[2] J. Chen,[2] R. M. Clark,[1] M. Cromaz,[1] P. Fallon,[1] J. Henderson,[4] R. V. F. Janssens,[8,9] M. D. Jones,[8] T. L. Khoo,[2] F. G. Kondev,[2] T. Lauritsen,[2] I. Y. Lee,[1] J. Li,[2] D. Potterveld,[2] C. Santamaria,[1] G. Savard,[2] D. Seweryniak,[2] S. Stolze,[2] and D. Weisshaar[10]

[1]*Nuclear Science Division, Lawrence Berkeley National Laboratory, Berkeley, California 94720, USA*
[2]*Physics Division, Argonne National Laboratory, Lemont, Illinois 60439, USA*
[3]*National Nuclear Data Center, Brookhaven National Laboratory, Upton, New York 11973, USA*
[4]*Lawrence Livermore National Laboratory, Livermore, California 94551, USA*
[5]*State Key Laboratory of Nuclear Physics and Technology, School of Physics, Peking University, Beijing 100871, China*
[6]*Yukawa Institute for Theoretical Physics, Kyoto University, Kyoto 606-8502, Japan*
[7]*Idaho National Laboratory, Idaho Falls, Idaho 83415, USA*
[8]*Department of Physics and Astronomy, University of North Carolina at Chapel Hill, Chapel Hill, North Carolina 27599, USA*
[9]*Triangle Universities Nuclear Laboratory, Duke University, Durham, North Carolina 27708, USA*
[10]*National Superconducting Cyclotron Laboratory, Michigan State University, East Lansing, Michigan 48824, USA*

The neutron-rich barium nuclei have been the subject of intense interest due to the enhanced octupole correlations they are predicted to exhibit. The observation of enhanced octupole collectivity in ^{144,146}Ba as measured in sub-barrier Coulomb excitation, consistent with static octupole deformation, has further heightened this interest. In the present work, these studies are extended to the neighboring odd-mass ^{143}Ba to investigate the interplay between single-particle and collective octupole degrees of freedom. A new measurement of the first $\frac{9}{2}^-$-state lifetime is also presented. Reflection-Asymmetric Triaxial Particle Rotor Model calculations indicate that the negative-parity bands in ^{143}Ba can be understood as a decoupled structure of $\nu h_{9/2}$ parentage, while the positive-parity bands are built on a decoupled octupole phonon. No evidence for $E3$ excitation is observed in this work, but an upper limit is placed on the $E3$ matrix element to the lowest octupole band.

I. INTRODUCTION

Just as quadrupole correlations among nucleons in atomic nuclei result in the breaking of spherical symmetry, octupole correlations may result in nuclei with reflection-asymmetric shapes [1–3]. However, the latter correlations are not as ubiquitous as quadrupole ones, requiring the presence of single-particle levels near the Fermi surface separated by $\Delta j = \Delta \ell = 3\hbar$; these conditions are satisfied for nucleon numbers $N, Z \approx 34$, 56, 88, and 134. Traditional signatures of octupole collectivity in even-even nuclei include the presence of interleaved positive- and negative-parity bands with enhanced $E1$ and $E3$ transitions between them, though the typically small $E1$ transition strengths are subject to cancellation effects induced by the single-particle shell structure, making $E1$ enhancement a less sensitive indicator [2,4]. Studies have revealed evidence for octupole collectivity in the radium ($Z = 88$) region [5,6] and in the neutron-rich lanthanides ($Z \sim 56$) [7–10]. The recent direct measurement of large $E3$ transition matrix elements in $^{144,146}_{56}$Ba, obtained via Coulomb excitation, may indicate stable octupole deformation [9,10] and has made this region of the nuclear chart a focus of particular interest.

While octupole correlations in even-even nuclei have received a great deal of attention, odd-mass systems present an important opportunity to study such correlations further. The delicate balance between blocking of pairing correlations and octupole particle-hole excitations, as well as polarization effects due to the odd neutron, may reveal details of the interplay between single-particle and collective degrees of freedom absent in even-even systems. Experimentally, the presence of parity doublets is an indicator of octupole correlations in odd-mass nuclei [11], in addition to enhanced $E3$ and potentially enhanced $E1$ transitions.

Here we report the results of low-energy Coulomb excitation of the odd-mass nucleus ^{143}Ba. The level structure of this nucleus has been investigated previously through β-decay [12,13] and spontaneous-fission [14–16] spectroscopic studies, while the ground-state properties have also been investigated by collinear laser spectroscopy [17–19]. Parity doublets and enhanced $E1$ transition rates have been observed in this nucleus [15], though the parity doublets are apparent only for higher excitation energies, in contrast to the octupole-deformed actinides where parity doublets are observed for the ground state [20]. Clearly, the most compelling evidence concerning octupole collectivity would come from direct

measurement of $E3$ transition matrix elements. In the present experiment, we place an upper limit on the lowest-lying $E3$ matrix element. We also determine several $E2$ matrix elements between negative-parity states. Reflection-Asymmetric Triaxial Particle Rotor Model [21–23] calculations are presented which interpret the negative-parity bands in ^{143}Ba as being based on the coupling of an $h_{9/2}$ neutron with a ^{142}Ba core, resulting in the $5/2^-$ ground state of ^{143}Ba. As we will show, the band structure can be understood in the rotation-aligned coupling scheme (RAL) [24] and the positive-parity bands as a RAL octupole phonon [25,26] coupled to the negative-parity states.

II. EXPERIMENTAL DETAILS

The experiment was performed at the Argonne Tandem Linear Accelerator System (ATLAS) facility at Argonne National Laboratory (ANL). The CAlifornium Rare Isotope Breeder Upgrade (CARIBU) [27] facility produced ^{143}Ba through fission of a $\sim$1 Ci ^{252}Cf source. The fission fragments were thermalized in a helium gas catcher before being injected into an electron beam ion source charge breeder and subsequently accelerated by ATLAS to a total energy of 627.8 MeV. The accelerated ^{143}Ba ions were impinged onto a 2-mg/cm^2 ^{208}Pb target to populate excited states through Coulomb excitation. A collimator was installed upstream of the target, and a HPGe detector was placed next to the beam dump immediately downstream of the target in order to monitor the beam current. Based on the intensity of the 211-keV γ ray emitted in the β decay of ^{143}Ba, the beam rate was estimated to be approximately 2500 ions per second.

Coulomb excitation events were identified and selected using the Compact Heavy Ion COunter (CHICO2) [28], which consisted of 20 Parallel Plate Avalanche Counters (PPACs) arranged around the target position. Ten PPACs were placed at forward angles and 10 at backward angles relative to the beam direction. Since Coulomb excitation results from quasielastic scattering, a coincidence condition was imposed that two PPACs separated by 180° in azimuthal angle must be hit within a certain time window, with at least one PPAC at forward polar angles. Beam and target particles can be distinguished and identified based on the time-of-flight difference from the target to the PPACs and the angle at which the particles are detected, as depicted in Fig. 1(a). The features corresponding to $A = 143$ and $A = 208$ particles are indicated in the figure.

The Gamma Ray Energy Tracking In-beam Nuclear Array (GRETINA) [29] surrounded CHICO2 in order to detect γ rays emitted after Coulomb excitation. GRETINA consisted of 11 Quad detector modules for this experiment, each containing four 36-fold segmented HPGe crystals, and covered polar angles from approximately 40° to 170° relative to the incoming beam direction. Doppler-corrected γ rays detected in coincidence with events in CHICO2 are presented in Fig. 1(b). The Doppler correction was calculated for particles with mass $A = 143$, assuming a midtarget reaction and quasielastic scattering. Transitions in ^{143}Ba are labeled by twice the spin of the initial and final states, while asterisks indicate lines from the isobaric beam contaminant ^{143}La.

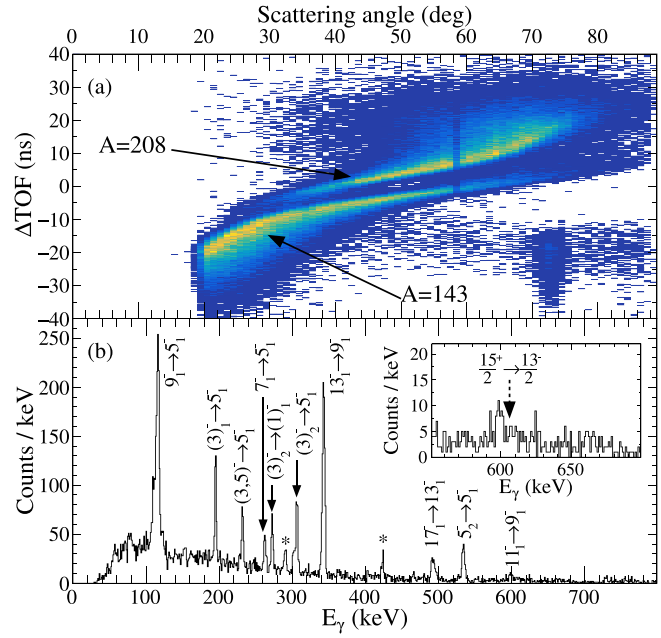

FIG. 1. (a) The particle identification spectrum measured in CHICO2. The scattering angle and time-of-flight difference between projectile ($A = 143$) and target ($A = 208$) nuclei are plotted on the horizontal and vertical axes, respectively. (b) Doppler-corrected γ-ray spectrum measured with GRETINA in coincidence with scattering events detected in CHICO2. Transitions are labeled by twice the spin of the initial and final states, while the asterisks indicate transitions which originate from ^{143}La. The inset shows the location of the $E1$ transition which would indicate population of positive-parity levels by $E3$ excitation.

A partial level scheme for ^{143}Ba is shown in Fig. 2. The solid arrows indicate transitions either observed in the present experiment or known to proceed based on published feeding patterns and branching ratios. Level energies and spin-parity

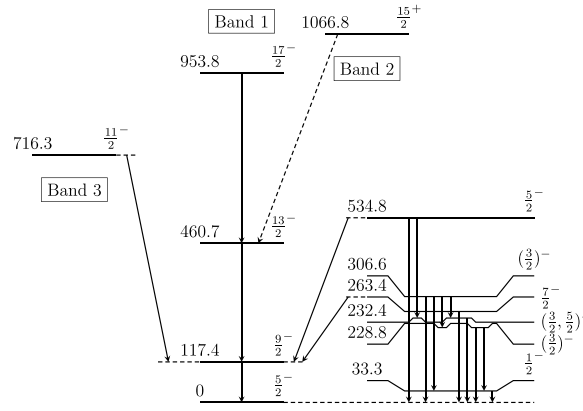

FIG. 2. A partial level scheme of ^{143}Ba. The solid arrows correspond to transitions observed in this work or known to have occurred based on published feeding patterns and branching ratios. Level energies and spin-parity assignments were taken from the latest ENSDF evaluation [30]. The $E1$ transition from the $\frac{15}{2}^+$ state was not observed in this experiment.

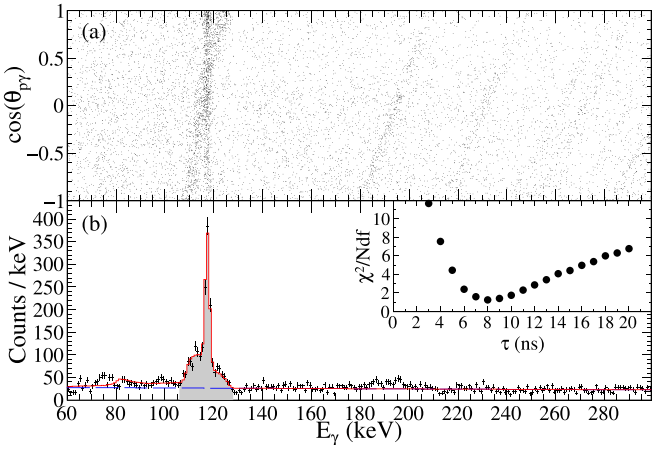

FIG. 3. (a) Cosine of the angle between scattered ^{143}Ba ions and γ rays detected in GRETINA plotted against the laboratory-frame γ-ray energy. The $\frac{9}{2}^- \rightarrow \frac{5}{2}^-$ transition decays both in flight and at rest, in contrast to the other transitions. (b) The results of the lifetime analysis of the $\frac{9}{2}^-$ state. The black crosses are the data with error bars, which were fit over the shaded region. The solid line is the best-fit simulation, and the background is indicated by the dashed line. The inset shows the reduced χ^2 distribution.

assignments have been taken from the latest data evaluation [30]. States associated with rotational bands built on the $\frac{11}{2}^-$ and $\frac{15}{2}^+$ states, in addition to another positive-parity band, are known but were not observed in the present experiment. The numbering of the bands used in the figure is identical to that used in Ref. [15], where bands 1 and 2 were assigned simplex $s = -i$ and bands 3 and 4 (not shown) were assigned simplex $s = +i$. The intensity of transitions in Fig. 1(b) indicates that the ground-state rotational band is strongly populated, while the transition from the 716.3-keV bandhead is observed only weakly. The transition from the positive-parity bandhead (the presumptive octupole band) at 1066.8 keV is not observed in the present work. The inset to Fig. 1(b) provides an expanded section of the γ-ray spectrum where this γ ray would appear, as indicated by the dashed arrow. The absence of this transition, with relatively little background in the region of interest, allows us to set a limit on the $\langle \frac{15}{2}^+ | E3 | \frac{9}{2}^- \rangle$ matrix element.

III. ANALYSIS AND RESULTS

A. Lifetime of the $\frac{9}{2_1}^-$ state

The first $\frac{9}{2}^-$ (hereafter $\frac{9}{2_1}^-$) state at 117.4 keV has a reported half-life of 3.5(8) ns [30], a weighted average of three values: 2.6(8) [16], 3.8(12) [31], and 6(2) ns [32]. However, Ref. [16] cites Ref. [31] but lists 3.8(1.2) ns as the mean lifetime (τ) instead of the half-life. This appears to be an error which has propagated into the literature, and thus only the latter two of the three values listed constitute independent measurements. While the remaining half-lives are statistically consistent with one another, the uncertainties are rather large. The present experiment provides a tighter constraint on this lifetime.

Figure 3(a) shows the cosine of the angle between the scattered ^{143}Ba nuclei and the emitted γ rays plotted against the laboratory-frame γ-ray energy detected in GRETINA. Two components are visible for the 117-keV line; The diagonal line is from γ rays emitted in flight, while the vertical one is due to photons emitted after the ^{143}Ba ions have come to rest. Note that the other photon-emission lines have only a Doppler-shifted component, and the lifetimes estimated by GOSIA (see Sec. III B) for all higher-energy levels from which transitions were observed in this experiment are less than 100 ps, which indicates that feeding effects can be safely neglected.

In order to determine the lifetime of the $\frac{9}{2_1}^-$ state, a simulation program was built using the Monte Carlo simulation toolkit Geant4 [33]. The simulation includes physical descriptions of the CHICO2 and GRETINA detectors as well as their supporting structures, such as the vacuum chamber for the PPACs and the frame which holds the GRETINA modules. Relativistic two-body kinematics calculations were implemented to model the Coulomb scattering events, including the angular distribution of scattered ^{143}Ba nuclei detected in coincidence with a 117-keV γ ray. The properties of the target and the beam were also incorporated, including the target width and material; the energy and energy width of the beam; the position, direction, size, and angular spread of the beam at the target position; and the energy and lifetime of the excited states of the scattered nuclei.

Simulated γ-ray spectra were generated for lifetimes in the range of 1–20 ns in one nanosecond steps. These spectra were fit to the laboratory-frame γ-ray spectrum, along with a background modeled by an exponential function, in order to determine which lifetime best reproduces the data as determined by the reduced χ^2 statistic. The result of this analysis is presented in Fig. 3(b). The data and error bars are shown in black, while the simulation with the best-fit lifetime is given by the solid red line. The background shape, which was fixed over the range shown, is represented by the dashed blue line. The inset shows the distribution of reduced χ^2 values. The minimum of this distribution is taken to be the lifetime, with the 1σ uncertainty determined by $\chi^2 + 1$. The resulting lifetime is $\tau = 8.5(6)$ ns, with both statistical and systematic effects included in the uncertainty.

B. Coulomb excitation analysis

Intensities for the observed γ rays were extracted in three scattering-angle ranges covering 25–40°, 40–55°, and 60–70° in the laboratory frame. The range covering 55–60° was shadowed by a support rib on the PPACs, and was therefore omitted. Possible unresolved lines from contaminants were investigated, and the 263-keV γ ray was found to be unresolved from a 261-keV γ transition in ^{143}La. The yield of this transition was corrected based on the observed intensity and branching ratio of the 291-keV line seen in the γ-ray spectrum, which originates from the same state as the 261-keV contaminant in ^{143}La [30]. The energy-dependent γ-ray detection efficiency of GRETINA was measured from 85 to 1408 keV using standard calibration sources of ^{60}Co, ^{137}Cs, ^{152}Eu, and ^{182}Ta and used to correct the measured intensities in order to determine the absolute γ-ray yield for each excited state in ^{143}Ba. The long lifetime of the $\frac{9}{2_1}^-$ state causes it to

TABLE I. Matrix elements extracted from the analysis performed with GOSIA. The values in the first and second rows are determined principally by the measured quadrupole moment of the ground state and the measured lifetime of the $\frac{9}{2}^-_1$ level, respectively. See text for details.

I_i^π	E_i (keV)	I_f^π	E_f (keV)	$\langle I_f\|E2\|I_i\rangle$ (eb)[a]	$B(E2)$ (or Q) (e^2b^2) (b^2)
$\frac{5}{2}^-_1$	0	$\frac{5}{2}^-_1$	0	−1.14(3)	−0.86(3)[b]
$\frac{9}{2}^-_1$	117.4	$\frac{5}{2}^-_1$	0	1.44(5)	0.21(2)[c]
$\frac{7}{2}^-_1$	263.4	$\frac{5}{2}^-_1$	0	0.21(3)	$5.6(17)\times10^{-3}$
$\frac{5}{2}^-_2$	534.8	$\frac{5}{2}^-_1$	0	0.32(10)	$1.7(10)\times10^{-2}$
$\frac{11}{2}^-_1$	716.3	$\frac{9}{2}^-_1$	117.4	0.59(13)	$2.9(13)\times10^{-2}$
$\frac{13}{2}^-_1$	460.7	$\frac{9}{2}^-_1$	117.4	1.86(12)	0.25(3)
$\frac{17}{2}^-_1$	953.8	$\frac{13}{2}^-_1$	460.7	2.00(27)	0.22(6)

[a]To convert from eb to Weisskopf units, divide by 6.7×10^{-2}.
[b]Primarily constrained by prior measurements [30].
[c]Primarily constrained by the $\frac{9}{2}^-$-state lifetime.

decay far from the target position, which modifies the efficiency with which the $\frac{9}{2}^- \rightarrow \frac{5}{2}^-$ transition is detected. This change in efficiency was estimated using the previously described Geant4 simulation, and the measured intensity was corrected accordingly.

The coupled-channels code GOSIA [34] was used to extract matrix elements from the observed γ-ray yields. The level scheme and data on known mixing ratios, branching ratios, and multipolarity were taken from the most recent data evaluation [30] and used as inputs for the calculation. In addition, the diagonal matrix elements and additional buffer levels above those shown in Fig. 2 were included in the level scheme input to GOSIA. The lifetime of the $\frac{9}{2}^-_1$ state reported in Sec. III A and the measured quadrupole moment of the ground state [30] were used as additional data inputs. Except for stretched $E2$ transitions and where otherwise noted in the data evaluation, transitions were assumed to be of mixed $M1+E2$ character. GOSIA was then used to fit the matrix elements to the experimental data. The 232.4-keV level has an uncertain spin of either $\frac{3}{2}$ or $\frac{5}{2}$; the minimization was performed with both values, but the results were not sensitive to this choice. The fit was repeated several times with the starting values of the matrix elements randomized in order to remove any bias based on the starting point of the minimization, although the nondiagonal $E2$ matrix elements in Band 1 were chosen to be positive. A good fit could be achieved in every case (reduced $\chi^2 < 1$), but only a subset of the matrix elements were well-constrained. These matrix elements are listed in Table I; the uncertainties reflect both those reported by GOSIA and the spread in the values across the randomized trials, which are taken as an additional systematic uncertainty. The $\langle\frac{5}{2}^-_1|E2|\frac{5}{2}^-_1\rangle$ and $\langle\frac{5}{2}^-_1|E2|\frac{9}{2}^-_1\rangle$ matrix elements are primarily constrained by the quadrupole moment of the ground state and the lifetime of the $\frac{9}{2}^-_1$ level, respectively.

As mentioned earlier, transitions were not observed from the positive-parity rotational bands, which precludes a determination of $E3$ transition strengths. However, the low γ-ray background in the region of interest does enable us to set an upper limit on the $\langle\frac{15}{2}^+|E3|\frac{9}{2}^-\rangle$ matrix element. To do so, the GOSIA calculations were repeated, but with the $E1$ and $E3$ matrix elements to the $\frac{15}{2}^+$ state included in the minimization. Upper limits corresponding to the 1σ uncertainty in the number of counts observed in each angular range were entered as data points to be fit. The results of the minimization indicated that the other matrix elements did not change with the addition of the transitions to the positive-parity band. The resulting limit on the $E3$ transition matrix element is $\langle\frac{15}{2}^+|E3|\frac{9}{2}^-\rangle < 0.5\ e\text{b}^{3/2}$.

IV. DISCUSSION

In order to discuss the implications of the present results, we consider the structure of ^{143}Ba from several perspectives. First, we present the results of new particle rotor model calculations and the insight gained by a detailed comparison to the experimental data. Next, we discuss the description of ^{143}Ba based on the alignment of the odd neutron and an octupole phonon, motivated by the comparison of the observed structure with the ^{142}Ba core. Finally, we return to the primary question of the degree of octupole collectivity in ^{143}Ba, and the implications of the established limit for the $E3$ transition matrix element.

A. RAT-PRM description of ^{143}Ba

Recently, a Reflection-Asymmetric Triaxial Particle Rotor Model (RAT-PRM) [21–23] has been developed and applied to studies of octupole correlations [35–37]. The detailed RAT-PRM formalism can be found in Refs. [21,22]. The total Hamiltonian is written

$$\hat{H} = \hat{H}_{\text{core}} + \hat{H}_{\text{s.p.}}, \tag{1}$$

where the core part is given by

$$\hat{H}_{\text{core}} = \sum_{k=1}^{3} \frac{(\hat{I}_k - \hat{j}_k)^2}{2\mathcal{J}_k} + \frac{1}{2}E(0^-)(1-\hat{P}_c), \tag{2}$$

where $\hat{I}_k$ and $\hat{j}_k$ are the angular momentum operators for the nucleus and the valence particles, $\mathcal{J}_k$ are the moments of inertia for irrotational flow, $E(0^-)$ is the core parity splitting parameter and $\hat{P}_c$ is the core parity operator. The intrinsic Hamiltonian is given by

$$\hat{H}_{\text{s.p.}} = -\tfrac{1}{2}\hbar\omega_0\nabla^2 + V(r;\theta,\varphi) + C\boldsymbol{l}\cdot\boldsymbol{s} + D[\boldsymbol{l}^2 - \langle\boldsymbol{l}^2\rangle_N], \tag{3}$$

with $-\frac{1}{2}\hbar\omega_0\nabla^2$ being the kinetic energy, $V(r;\theta,\varphi)$ the reflection-asymmetric triaxially deformed potential [21], $C\boldsymbol{l}\cdot\boldsymbol{s}$ the spin-orbit coupling term, and the standard $D[\boldsymbol{l}^2 - \langle\boldsymbol{l}^2\rangle_N]$ term [38]. The single-particle energy can be obtained by diagonalizing $\hat{H}_{\text{s.p.}}$ and the pairing correlations taken into account by the Bardeen-Cooper-Schrieffer approximation [21,39].

The Hamiltonian $\hat{H}$ is diagonalized numerically in the symmetrized strong-coupled basis with good parity and an-

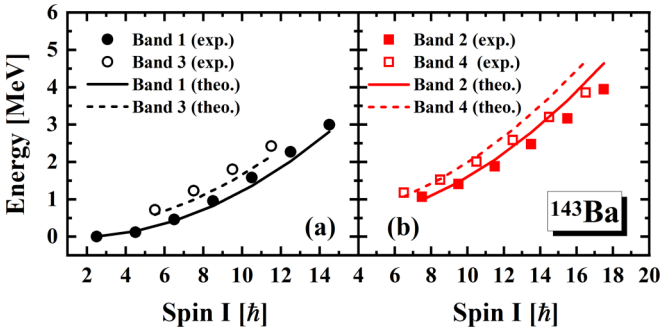

FIG. 4. The energies $E(I)$ for the negative-parity bands 1 and 3 (a) as well as for the positive-parity bands 2 and 4 (b) in ^{143}Ba by RAT-PRM (lines) in comparison with the available data [15] (symbols).

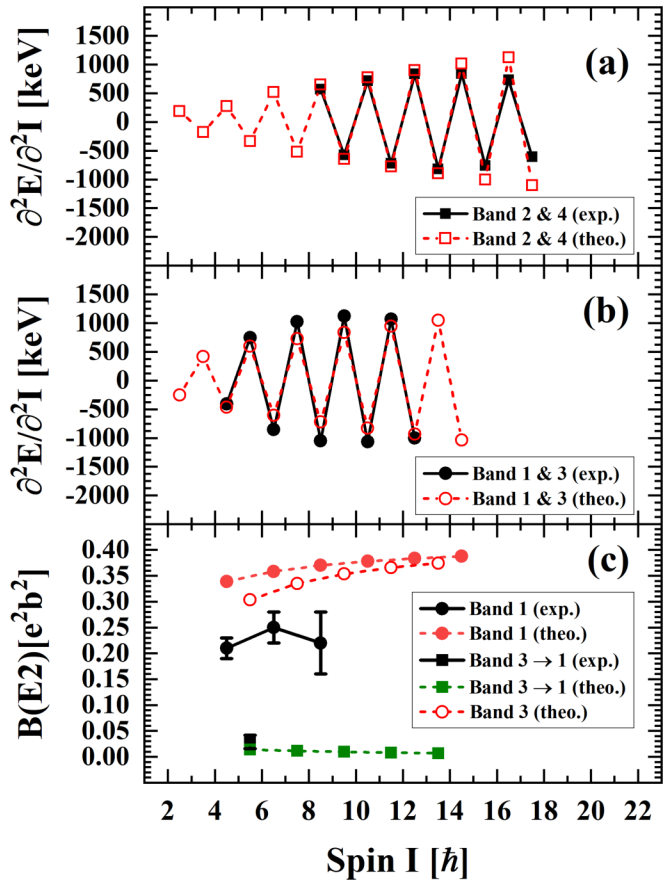

FIG. 5. The second derivative of the level energies with respect to spin as a function of spin, also known as the staggering plot, for (a) the positive-parity bands 2 and 4 and (b) the negative-parity bands 1 and 3 in ^{143}Ba by RAT-PRM (red symbols) in comparison with the available data [15] (black symbols). Panel (c) shows the experimental intraband $B(E2)$ of band 1 and the interband $B(E2)$ between band 3 and 1 obtained from the present work in comparison with the RAT-PRM results (red and green symbols).

gular momentum [21], giving rise to the desired eigenvalues and eigenfunctions. One can then calculate the reduced electromagnetic transition probabilities, etc. [21].

The quadrupole and octupole deformations are microscopically and self-consistently obtained from covariant density functional theory [40]. From the functional PC-PK1 [41], a three-dimensional lattice calculation [42,43] for the configuration $\nu h_{9/2}$ provides $\beta_2 = 0.2$, $\gamma = 0^\circ$, and $\beta_3 = 0.115$. With these deformation parameters, the single-particle Hamiltonian $\hat{H}_{\text{s.p.}}$ with parameters κ, μ in Ref. [44] is solved in the harmonic oscillator basis [45]. The single-particle space is truncated with six states above and six below the Fermi level. Increasing the single-particle model space does not influence the band structure in the present work. The pairing correlations are taken into account by the empirical pairing gap formula $\Delta = 12/\sqrt{A}$ MeV. For the core part, the moment of inertia $\mathcal{J}_0 = 30\ \hbar^2/\text{MeV}$, the core parity splitting parameter $E(0^-) = 0.45$ MeV, and the Coriolis attenuation $\xi = 0.6$ were adjusted to the experimental energy spectra. For the calculations of the electromagnetic transitions, the intrinsic dipole, quadrupole, and octupole moments are taken to be $0.0006 * AZe\beta_2\beta_3$, $(3/\sqrt{5\pi})R_0^2 Z\beta_2$, and $-(6/7)R_0^3 Ze\beta_3$, respectively [46].

In Fig. 4, the energies $E(I)$ calculated by the RAT-PRM for the negative-parity bands 1 and 3 as well as for the positive-parity bands 2 and 4 are compared with the available data, where the numbering of the bands is the same as in Ref. [15]. As demonstrated in Fig. 4, the experimental spectra for these bands are reproduced well within the RAT-PRM calculations.

Figures 5(a) and 5(b) provide the so-called staggering plots—the second derivative of the excited-state energies as a function of spin—for the positive- and negative-parity bands, respectively. The results calculated by the RAT-PRM are compared with the available data [15]. The RAT-PRM calculations reproduce the staggering behavior well for both positive- and negative-parity bands.

Figure 5(c) compares the $B(E2)$ transition strengths determined in the present work with the RAT-PRM results, both for intraband and interband transitions. The observed interband $E2$ transition between negative-parity bands 3 and 1 is small and can be well reproduced by the RAT-PRM calculations. For the intraband $E2$ transitions of band 1, the calculated results slightly overestimate the experimental data.

The octupole deformation β_3 contributes to both the dipole and the octupole moments, which affects the calculated $B(E3)$ strength and the $B(E1)/B(E2)$ ratios. The calculated deformation parameters $(\beta_2, \beta_3) = (0.2, 0.115)$ result in $B(E1)/B(E2)$ ratios which underestimate the reported data [15], while the $B(E3)$ transition strength exceeds the upper limit determined in this work. In order to explore the sensitivity of these ratios to the octupole deformation, β_3 was increased from the value obtained from covariant density functional theory to several values shown in Table II. The energy levels, level staggering, and quadrupole transition strengths remained stable while varying β_3. While the $B(E1)/B(E2)$ ratios did increase as a function of the octupole deformation, agreement with the experimental data could not be obtained even with the largest β_3 values. In contrast, the calculated $B(E3)$ transition rates further overestimate the experimental upper limit. A linear extrapolation suggests that $\beta_3 < 0.06$ satisfies the experimental limit on the $B(E3)$ value.

TABLE II. $B(E3; \frac{9}{2}^- \rightarrow \frac{15}{2}^+)$ values calculated in the RAT-PRM for the deformation parameters indicated. The calculated values all exceed the experimental limit.

			$B(E3)$ (e^2b^3)[a]	
I_i^π	I_f^π	(β_2, β_3)	Theory	Experiment
$\frac{9}{2}^-_1$	$\frac{15}{2}^+_1$	(0.2,0.115)	0.09283	<0.025
		(0.2,0.14)	0.1382	
		(0.2,0.17)	0.2082	
		(0.2,0.20)	0.2932	

[a]To convert from e^2b^3 to Weisskopf units, divide by 1.2×10^{-3}.

B. Particle and phonon alignment in ^{143}Ba

The properties of the quartet of highly interconnected bands in ^{143}Ba have been suggested to indicate stable octupole deformation [15]. However, other interpretations are possible, such as the presence of an octupole phonon. Indeed, given the modest rotational character of ^{142}Ba [$E(4^+)/E(2^+) \approx 2.3$], the similarity of the energy spacings of the like-parity bands in ^{143}Ba to the energies of the ^{142}Ba core, and the strong level staggering in Figs. 5(a) and 5(b), one might expect a predominantly rotation-aligned coupling [24] between the odd neutron and the core, with an additional contribution from octupole correlations.

In the PRM, the ratio of the Coriolis matrix elements $H_c \sim \hbar^2 I j/\mathcal{J}$ to the intrinsic level spacings $\Delta E \sim \beta_2 \hbar\omega_0$ serves as a control parameter defining the characteristics of the coupling between collective and intrinsic angular momenta. For $H_c/\Delta E \ll 1$, the particle remains strongly coupled to the core, maintaining the projection of its angular momentum on the symmetry axis, Ω, as a good quantum number. When $H_c/\Delta E \gg 1$, a RAL coupling limit is anticipated [24,47]. In this case, the *yrast* band has spins $I = j,\ j+2,\ j+4,\ \ldots$ and energy spacings equal to those of the core; this type of band is referred to as a decoupled band. The Coriolis Ω-mixed wave function can be approximated by [47]:

$$\psi_{I,\mathrm{yrast}} \approx \sum_{\Omega} d^{9/2}_{9/2,\Omega}\left(\frac{\pi}{2}\right)|I\Omega\rangle, \tag{4}$$

where $d^j_{m'm}(\theta)$ is the Wigner d-matrix. Given the small quadrupole deformation of ^{142}Ba, for which the core $\mathcal{J}$ is small, and the large j of the case at hand, the RAL limit is dominant. Note, however, that the $5/2^-$ ground state is not a member of the decoupled band, which starts at the $\frac{9}{2}^-$ bandhead.

In an axially deformed nucleus, octupole vibrations can manifest themselves with the appearance of oscillations of the $Y^\nu_{\lambda=3}(\theta,\phi)$ field, having $\nu^\pi = 0^-, 1^-, 2^-$, and 3^- projections on the symmetry axis [26]. In analogy to the discussion above for the quasi-neutron, it is also anticipated that the phonon will align its angular momentum with the rotation axis due to the Coriolis interaction [25,26], giving rise to a decoupled octupole-phonon band. In this limit, the wave functions of the lowest octupole band can be approximated as

$$\psi_{I,\mathrm{octupole}} \approx \sum_{\nu} d^3_{3,\nu}\left(\frac{\pi}{2}\right)|I\nu\rangle, \tag{5}$$

with the energies following those of the core:

$$E(I+2) - E(I) \approx E(R+2) - E(R). \tag{6}$$

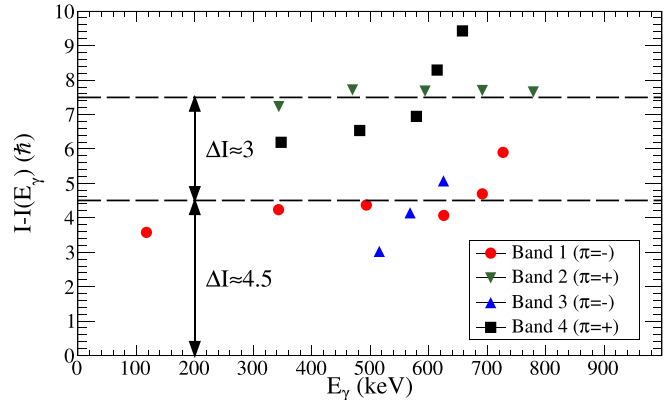

FIG. 6. The alignment plot for ^{143}Ba. The negative-parity levels, shown by the circles and upright triangles, exhibit significant alignment compared to the ground-state band of ^{142}Ba, consistent with a decoupled band. The further alignment of the positive-parity bands (squares and inverted triangles) by three units of angular momentum suggests that they are based on the presence of an aligned octupole phonon. See text for details.

We explore this idea in Fig. 6 with the alignment plot for the four bands identified in ^{143}Ba relative to the ground state band of ^{142}Ba. Here $I(E_\gamma)$ represents the spin of ^{142}Ba as a function of γ-ray energy; the vertical axis of the plot is the difference between the spin of a given level in ^{143}Ba and this function, while the horizontal axis is the γ-ray transition energy in ^{143}Ba. A strong alignment of the negative-parity bands, characteristic of a decoupled band [47], is clearly seen. We also see that the positive-parity states have even larger alignment than the negative-parity levels. The excess of about three units of alignment relative to the negative-parity states suggests that they are based on an aligned octupole phonon. This is in accord with the conclusions in Ref. [48] assigning an octupole vibrational character to most nuclei with $Z \approx 56$ and $N \approx 88$, similar to the cases of the radon isotopes and the more neutron-rich isotopes of Ra, Th and U. Therefore, in ^{143}Ba, Fig. 6 suggests a doubly decoupled structure (neutron and phonon) for the octupole states.

C. The limit on the $E3$ transition matrix element in the aligned phonon picture

Returning to the motivating question of the degree of octupole collectivity in ^{143}Ba, we now explore the meaning of the experimental limit on the $E3$ transition matrix element. The small value inferred for β_3 in Sec. IV A indicates that the assumption of static octupole deformation may not be appropriate for ^{143}Ba, and suggests instead a dynamic nature. This is supported by the $3\hbar$ alignment of the octupole phonon discussed in Sec. IV B. In fact, recent results [49]

in the framework of the *sdf*-Interacting Boson Model, with a mapped Hamiltonian determined from (β_2, β_3)-constrained self-consistent mean-field calculations, predict for ^{142,143}Ba a weakly deformed quadrupole shape with $(\beta_2, \beta_3) \approx (0.14, 0)$ and $B(E3; \frac{9}{2}^- \rightarrow \frac{15}{2}^+) = 0.022\ e^2\mathrm{b}^3$. The predicted $B(E3)$ value is quite close to the experimental upper limit, while the quadrupole deformation can be calculated from the $B(E2; \frac{9}{2}^- \rightarrow \frac{5}{2}^-)$ transition strength [50]:

$$\beta_2 = \frac{4\pi}{3ZR_0^2}\sqrt{B(E2\uparrow)/e^2}, \tag{7}$$

with $R_0 = 1.2A^{1/3}$. Using the $B(E2)$ strength in Table I gives $\beta_2 = 0.112(5)$, only slightly smaller than predicted.

The RAL coupling scheme of the aligned phonon picture corresponds to a $\pi/2$ rotation from the symmetry to the rotation axis. Adopting this as our $\hat{3}$ axis, we can write

$$\langle 3^-|E3|0^+\rangle = \sqrt{\frac{7}{16\pi}}eQ_3. \tag{8}$$

From Eq. (5) it follows that

$$Q_3 = \sum_\nu d^3_{3,\nu}\left(\frac{\pi}{2}\right)Q^0_{3,\nu} \tag{9}$$

in terms of the moments of each individual phonon component, $Q^0_{3,\nu}$. It is important to note that Eq. (9) will, in general, result in a value which is larger than any of the components in the sum. Therefore, one should be cautious in making an assignment of octupole deformation directly from the Q_3 moment.

In ^{143}Ba, based on the observed alignment relative to the ground-state band, we have argued earlier that the lowest octupole band can be explained as a doubly decoupled structure having both the single particle and the phonon aligned with the rotation axis. In this case, with the odd $h_{9/2}$ neutron effectively being a spectator with respect to the alignment of the octupole phonon, the $E3$ matrix element can be expressed in terms of Eq. (8):

$$\left\langle \frac{15}{2}^+\middle|E3\middle|\frac{9}{2}^-\right\rangle \approx \langle 3^-|E3|0^+\rangle = \sqrt{\frac{7}{16\pi}}eQ_3. \tag{10}$$

Thus, the upper limit on the $E3$ transition matrix element implies a moment $Q_3 \leqslant 1330\,e\,\mathrm{fm}^3$. While there is some overlap with $Q_3 = 1730(^{+450}_{-620})\,e\,\mathrm{fm}^3$ for ^{144}Ba, the smaller value of our upper limit may indicate a reduction in octupole collectivity consistent with that of ^{142}Ba, for which the comparably high energy of the 3^- level provides evidence. Using similar arguments, one can show that in this coupling scheme the $B(E1)/B(E2)$ ratios in ^{143}Ba should follow those of the core. This appears to be in line with the experimental observations [7,14,15].

As a final remark, it is worth noting that there is currently still uncertainty regarding the low-lying level scheme of ^{143}Ba. Many levels below 1 MeV in excitation energy [30] have unknown spins and parities. While no connection between these levels and the positive-parity bands is known at the present time, it is conceivable that such transitions will be discovered in the future. This could impact the interpretation of the data that we have presented here; for example, $E3$ excitation pathways could exist which compete with the $\frac{9}{2}^- \rightarrow \frac{15}{2}^+$ excitation, thus fragmenting the $E3$ strength. However, given the difficulty of drawing definite conclusions on the basis of speculation about these unidentified levels, we have restricted our discussion to what is known at this time. Future experiments to fully elucidate the level scheme—both the spin-parity assignments of the excited states and the multipolarity of the γ rays—would be a great help in achieving a complete understanding of this nucleus.

TABLE III. The efficiency-corrected γ-ray yields measured in this experiment, separated into the angular ranges used in the analysis. Y_1 corresponds to the angular range 25–40°, Y_2 to 40–55°, and Y_3 to 60–70°.

I_i^π	I_f^π	E_γ (keV)	Y_1	Y_2	Y_3
$\frac{9}{2}^-$	$\frac{5}{2}^-$	117.3	8952(462)	6077(379)	1610(178)
$(\frac{3}{2})^-$	$\frac{5}{2}^-$	228.8	154(65)	171(49)	34(29)
$(\frac{3}{2})^-$	$(\frac{1}{2})^-$	195.6	1077(113)	784(102)	224(57)
$(\frac{3}{2}, \frac{5}{2})^-$	$\frac{5}{2}^-$	232.4	531(94)	463(131)	146(45)
$\frac{7}{2}^-$	$\frac{5}{2}^-$	263.4	412(85)	259(86)	87(46)
$(\frac{3}{2})^-$	$\frac{5}{2}^-$	306.4	933(116)	878(115)	362(68)
$(\frac{3}{2})^-$	$(\frac{1}{2})^-$	272.7	597(109)	509(94)	123(46)
$\frac{13}{2}^-$	$\frac{9}{2}^-$	343.3	1682(144)	3157(188)	1353(121)
$\frac{5}{2}^-$	$\frac{5}{2}^-$	534.8	657(95)	679(97)	362(73)
$\frac{5}{2}^-$	$(\frac{3}{2}, \frac{5}{2})^-$	302.5	271(85)	216(77)	18(31)
$\frac{11}{2}^-$	$\frac{9}{2}^-$	598.9	84(41)	143(51)	36(24)
$\frac{17}{2}^-$	$\frac{13}{2}^-$	493.1	87(48)	458(100)	306(62)

V. SUMMARY

In summary, we have reported here several experimental results pertaining to the structure of ^{143}Ba. We have provided a new measurement of the lifetime of the $\frac{9}{2}^-_1$ state and reduced the uncertainty of this value significantly. We also provide several $E2$ matrix elements connecting members of low-lying rotational bands. RAT-PRM calculations are presented, which are able to reproduce the level staggering well and the $B(E2)$ values fairly well, but overestimate the octupole collectivity. Alignment plots and the energy-level staggering indicate that ^{143}Ba is well described by a decoupled band structure, which the RAT-PRM calculations indicate is based on a $\nu h_{9/2}$ configuration. Furthermore, we propose that the octupole collectivity in this nucleus can be attributed to an aligned octupole phonon, and that ^{143}Ba can thus be considered to exhibit a doubly decoupled structure; i.e. a decoupled neutron and a decoupled octupole phonon coupled to the weakly quadrupole-deformed ^{142}Ba core.

ACKNOWLEDGMENTS

The authors thank the ATLAS operations staff at ANL for their hard work in providing us with the radioactive ^{143}Ba

beam. We also acknowledge enlightening discussions with L. P. Gaffney, P. A. Butler, and S. Frauendorf. This material is based on work supported by the U.S. Department of Energy, Office of Science, Office of Nuclear Physics under Contracts No. DE-AC02-05CH11231 (LBNL), No. DE-AC02-06CH11357 (ANL), and No. DE-AC02-98CH10886 (BNL) and Grants No. DE-FG02-97ER41041 (UNC) and No. DE-FG02-97ER41033 (TUNL). GRETINA was funded by the U.S. DOE, Office of Science, Office of Nuclear Physics, and operated by the ANL contract number above and by Contract No. DE-AC02-05CH11231 (LBNL). Work at LLNL was performed under DOE Contract No. DE-AC52-07NA27344, and at INL under Contract No. DE-AC07-05ID14517. Y.Y.W. and J.M. acknowledge the support of the National Natural Science Foundation of China (Grants No. 11875075, No. 11935003, No. 11975031, and No. 11621131001), the National Key R&D Program of China (Contracts No. 2018YFA0404400 and No. 2017YFE0116700), the State Key Laboratory of Nuclear Physics and Technology, Peking University (No. NPT2020ZZ01), and the China Postdoctoral Science Foundation under Grant No. 2020M670014. This research used resources of the ATLAS facility at ANL, which is a DOE Office of Science User Facility.

APPENDIX: EFFICIENCY-CORRECTED γ-RAY YIELDS

The efficiency-corrected γ-ray yields measured in this experiment are provided in Table III.

[1] I. Ahmad and P. A. Butler, Ann. Rev. Nucl. Part. Sci. **43**, 71 (1993).
[2] P. A. Butler and W. Nazarewicz, Rev. Mod. Phys. **68**, 349 (1996).
[3] P. A. Butler, J. Phys. G **43**, 073002 (2016).
[4] G. Leander, W. Nazarewicz, G. Bertsch, and J. Dudek, Nucl. Phys. A **453**, 58 (1986).
[5] L. P. Gaffney *et al.*, Nature **497**, 199 (2013).
[6] H. J. Wollersheim *et al.*, Nucl. Phys. A **556**, 261 (1993).
[7] W. Urban *et al.*, Nucl. Phys. A **613**, 107 (1997).
[8] T. Kibédi and R. H. Spear, At. Data Nucl. Data Tables **80**, 35 (2002).
[9] B. Bucher *et al.*, Phys. Rev. Lett. **116**, 112503 (2016).
[10] B. Bucher *et al.*, Phys. Rev. Lett. **118**, 152504 (2017).
[11] R. R. Chasman, Phys. Lett. B **96**, 7 (1980).
[12] M. Rapaport and A. Gayer, Int. J. Appl. Radiat. Isot. **36**, 689 (1985).
[13] J. D. Robertson, P. F. Mantica, S. H. Faller, C. A. Stone, E. M. Baum, and W. B. Walters, Phys. Rev. C **40**, 2804 (1989).
[14] S. J. Zhu *et al.*, Phys. Lett. B **357**, 273 (1995).
[15] S. J. Zhu, J. H. Hamilton, A. V. Ramayya, E. F. Jones, J. K. Hwang, M. G. Wang, X. Q. Zhang, P. M. Gore, L. K. Peker, G. Drafta, B. R. S. Babu, W. C. Ma, G. L. Long, L. Y. Zhu, C. Y. Gan, L. M. Yang, M. Sakhaee, M. Li, J. K. Deng, T. N. Ginter, C. J. Beyer, J. Kormicki, J. D. Cole, R. Aryaeinejad, M. W. Drigert, J. O. Rasmussen, S. Asztalos, I. Y. Lee, A. O. Macchiavelli, S. Y. Chu, K. E. Gregorich, M. F. Mohar, G. M. Ter-Akopian, A. V. Daniel, Y. T. Oganessian, R. Donangelo, M. A. Stoyer, R. W. Lougheed, K. J. Moody, J. F. Wild, S. G. Prussin, J. Kliman, and H. C. Griffin, Phys. Rev. C **60**, 051304(R) (1999).
[16] A. G. Smith *et al.*, Phys. Lett. B **453**, 206 (1999).
[17] A. C. Mueller, F. Buchinger, W. Klempt, E. W. Otten, R. Neugart, C. Ekström, and J. Heinemeier, Nucl. Phys. A **403**, 234 (1983).
[18] K. Wendt, S. A. Ahmad, C. Ekström, W. Klempt, R. Neugart, and E. W. Otten, Z. Phys. A **329**, 407 (1988).
[19] R. Neugart, F. Buchinger, W. Klempt, A. C. Mueller, E. W. Otten, C. Ekström, and J. Heinemeier, Hyperfine Interact. **9**, 151 (1981).
[20] G. Leander and R. Sheline, Nucl. Phys. A **413**, 375 (1984).
[21] Y. Y. Wang, S. Q. Zhang, P. W. Zhao, and J. Meng, Phys. Lett. B **792**, 454 (2019).
[22] Y. P. Wang, Y. Y. Wang, and J. Meng, Phys. Rev. C **102**, 024313 (2020).
[23] Y. Wang, X. Wu, S. Zhang, P. Zhao, and J. Meng, Sci. Bull. (2020).
[24] F. S. Stephens, Rev. Mod. Phys. **47**, 43 (1975).
[25] P. Vogel, Phys. Lett. B **60**, 431 (1976).
[26] A. Bohr and B. R. Mottelson, *Nuclear Struture Vol. II* (World Scientific, Singapore, 1998).
[27] G. Savard, S. Baker, C. Davids, A. F. Levand, E. F. Moore, R. C. Pardo, R. Vondrasek, B. J. Zabransky, and G. Zinkann, Nucl. Instrum. Methods B **266**, 4086 (2008).
[28] C. Y. Wu, D. Cline, A. Hayes, R. S. Flight, A. M. Melchionna, C. Zhou, I. Y. Lee, D. Swan, R. Fox, and J. T. Anderson, Nucl. Instrum. Methods A **814**, 6 (2016).
[29] S. Paschalis *et al.*, Nucl. Instrum. Methods A **709**, 44 (2013).
[30] E. Browne and J. K. Tuli, Nucl. Data Sheets **113**, 715 (2012).
[31] F. Schussler, J. Blachot, E. Monnand, B. Fogelberg, S. H. Feenstra, J. van Klinken, G. Jung, and K. D. Wünsch, Z. Phys. A **290**, 359 (1979).
[32] R. G. Clark, L. E. Glendenin, and W. L. Talbert, Jr., in *Proceedings of the 3rd Symposium on Physics and Chemistry of Fission*, Vol. 2 (IAEA, Vienna, 1974), p. 221.
[33] S. Agostinelli *et al.*, Nucl. Instrum. Methods A **506**, 250 (2003).
[34] T. Czosnyka, D. Cline, and C. Y. Wu, Bull. Am. Phys. Soc. **28**, 745 (1983).
[35] S. Frauendorf and J. Meng, Nucl. Phys. A **617**, 131 (1997).
[36] J. Meng, J. Peng, S. Q. Zhang, and S.-G. Zhou, Phys. Rev. C **73**, 037303 (2006).
[37] S. Guo *et al.*, Phys. Lett. B **807**, 135572 (2020).
[38] P. Ring and P. Schuck, *The Nuclear Many-body Problem* (Springer Science & Business Media, New York, 2004).
[39] S. Q. Zhang, B. Qi, S. Y. Wang, and J. Meng, Phys. Rev. C **75**, 044307 (2007).
[40] J. Meng, ed., *Relativistic Density Functional for Nuclear Structure*, International Review of Nuclear Physics, Vol. 10 (World Scientific, Singapore, 2016).
[41] P. W. Zhao, Z. P. Li, J. M. Yao, and J. Meng, Phys. Rev. C **82**, 054319 (2010).

[42] Z. X. Ren, S. Q. Zhang, and J. Meng, Phys. Rev. C **95**, 024313 (2017).
[43] Z. X. Ren, S. Q. Zhang, P. W. Zhao, N. Itagaki, J. A. Maruhn, and J. Meng, Sci. China-Phys. Mech. Astron. **62**, 112062 (2019).
[44] S. G. Nilsson, C. F. Tsang, A. Sobiczewski, Z. Szymański, S. Wycech, C. Gustafson, I.-L. Lamm, P. Möller, and B. Nilsson, Nucl. Phys. A **131**, 1 (1969).
[45] Y. Y. Wang and Z. X. Ren, Sci. China Phys. Mech. Astron. **61**, 082012 (2018).
[46] G. A. Leander and Y. S. Chen, Phys. Rev. C **37**, 2744 (1988).
[47] F. S. Stephens, R. M. Diamond, and S. G. Nilsson, Phys. Lett. B **44**, 429 (1973).
[48] P. A. Butler, Proc. R. Soc. A. **476**, 0202 (2020).
[49] K. Nomura, T. Nikšić, and D. Vretenar, Phys. Rev. C **97**, 024317 (2018).
[50] S. Raman, C. Nestor, and P. Tikkanen, At. Data Nucl. Data Tables **78**, 1 (2001).